



# Simulating tsunami propagation in fjords with long-wave models

F. Løvholt<sup>1,2</sup>, S. Glimsdal<sup>1,2</sup>, P. Lynett<sup>3</sup>, and G. Pedersen<sup>1</sup>

<sup>1</sup>University of Oslo, Department of Mathematics, P.O. Box 1072, Blindern 0316, Oslo, Norway

<sup>2</sup>Norwegian Geotechnical Institute, P.O. Box 3930, 0806 Ullevål Stadion, Oslo, Norway

<sup>3</sup>Sonny Astani Department of Civil and Environmental Engineering, University of Southern California, Los Angeles, USA

Correspondence to: F. Løvholt (finn.lovholt@ngi.no)

Received: 12 July 2014 – Published in Nat. Hazards Earth Syst. Sci. Discuss.: 1 August 2014

Revised: – – Accepted: 8 March 2015 – Published: 27 March 2015

**Abstract.** Tsunamis induced by rock slides constitute a severe hazard towards coastal fjord communities. Fjords are narrow and rugged with steep slopes, and modeling the short-frequency and high-amplitude tsunamis in this environment is demanding. In the present paper, our ability (and the lack thereof) to simulate tsunami propagation and run-up in fjords for typical wave characteristics of rock-slide-induced waves is demonstrated. The starting point is a 1 : 500 scale model of the topography and bathymetry of the southern part of Storfjorden fjord system in western Norway. Using measured wave data from the scale model as input to numerical simulations, we find that the leading wave is moderately influenced by nonlinearity and dispersion. For the trailing waves, dispersion and dissipation from the alongshore inundation on the traveling wave become more important. The tsunami inundation was simulated at the two locations of Hellesylt and Geiranger, providing a good match with the measurements in the former location. In Geiranger, the most demanding case of the two, discrepancies are larger. The discrepancies may be explained by a combinations of factors, such as the accumulated errors in the wave propagation along large stretches of the fjord, the coarse grid resolution needed to ensure model stability, and scale effects in the laboratory experiments.

genic power. Examples of rock-slide-induced tsunamis include the 1958 Lituya Bay event (Miller, 1960), the 1971 Yanahuin Lake (Plafker and Eyzaguirre, 1979), the 1783 Scilla landslide (Tinti and Guidoboni, 1988), and the video-documented 2007 Aisén fjord series of rock slides in southern Chile (Sepúlveda and Serey, 2009). In Norway, three major tsunamis struck communities in Loen (1904, 1936) and Tafjord (1934), causing altogether 175 fatalities (Jørstad, 1968; Harbitz et al., 1993). In Storfjorden, western Norway, a number of older rock-slide events are evident from high-resolution seabed surveys (Blikra et al., 2005). Some of the events are located immediately offshore the presently unstable Åknes rock slope. Due to large relative movements up to 20 cm per year (Oppikofer et al., 2010) and unstable volumes exceeding several million cubic meters, Åknes is presently considered the most hazardous potential tsunamigenic rock slope in Norway.

Fjords and narrow lakes may be effective waveguides as they channel the wave energy, involving less radial spread than the tsunamis propagating in the open sea. Due to the impulsive nature of the rock-slide water impact, the wave evolution becomes dispersive. Traditional tsunami models based on the shallow water formulation (e.g., Titov and Synolakis, 1995; Imamura, 1996; Titov and Synolakis, 1997; LeVeque and George, 2008) do not include dispersion, and dispersive wave models such as those based on the Boussinesq formulation (Madsen and Sørensen, 1992; Nwogu, 1993; Wei et al., 1995; Lynett et al., 2002; Madsen et al., 2003) constitute better alternatives. New Boussinesq models have been formulated using the shock-capturing approximate Riemann solvers in combination with TVD (total variation diminishing limiters, e.g. Erduran et al., 2005; Kim et al., 2009; Kim and Lynett, 2011; Shi et al., 2012; Tonelli and Petti, 2012).

## 1 Introduction

Subaerial landslides originating from rock-slope failures are effective wave generators that impact the water body at high and initially supercritical speeds (see e.g., Fritz et al., 2004; Heller et al., 2008). They occur in fjords, lakes, or rivers, and with large volumes they may have significant tsunami-

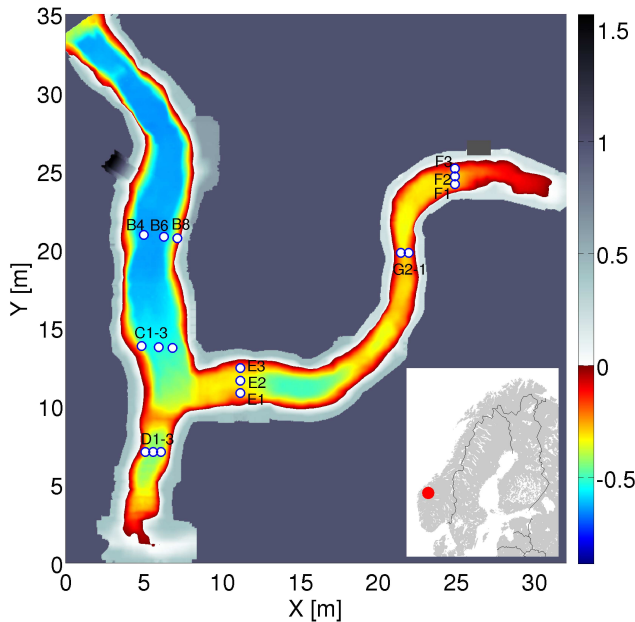


**Figure 1.** Applied bathymetry derived from lidar measurements of the scale model of Storfjorden. A subset of the time series gauges that concur with the resistant wave gauges reported in Lindstrøm et al. (2014) are also depicted. The location of the landslide source in the experiments of Lindstrøm et al. (2014) is north of the B gauges ( $Y = 25$  m). The inset indicates the geographical location of the fjord that the 1 : 500 scale model is mimicking.

Yet, recent work has demonstrated that the fjords constitute demanding test cases for Boussinesq models involving possible instabilities. The instabilities are for instance linked to the terms related to steep bathymetric slopes (Løvholt and Pedersen, 2009) or strong nonlinearity and run-up (Løvholt et al., 2013). As a consequence, the fully nonlinear Boussinesq models with run-up are yet to be deployed for simulating tsunamis in fjords.

Due to the fjords being narrow and dominated by rugged steep slopes, tsunamis inundate the coastlines as they propagate. At the same time the tsunami may exhibit breaking. Both of the latter effects should be properly accounted for in the propagation model, which obviously constitutes a challenge. Yet such effects remain unquantified in the tsunami literature. Recently, Harbitz et al. (2014) simulated potential tsunamis in Storfjorden using the dispersive wave model GloBouss (Løvholt et al., 2008; Pedersen and Løvholt, 2008). As run-up and breaking effects are not included in GloBouss, adaptation of the local bathymetry was necessary to facilitate the simulations. In the present paper, we investigate how run-up, nonlinearity, and dispersion influence the wave propagation. The starting point is a 1 : 500 scale model of the topography and bathymetry of Storfjorden (Fig. 1). The experimental setup, which is rigorously explained by Lindstrøm et al. (2014), includes a rigid landslide block source released at  $t = 0$  s immediately after impacting

undisturbed water level, providing time series of the resulting surface elevations in the fjord basin. Using the measured time series to construct input conditions to our numerical models, we ensure that the amplitudes and wave periods mimic those generated by the subaerial landslide. Employing the fully nonlinear Coulwave model, including run-up (Lynett et al., 2002; Kim et al., 2009; Kim and Lynett, 2011) and GloBouss (Pedersen and Løvholt, 2008; Løvholt et al., 2008) in various modes, we investigate the importance of different parameters and formulations on the wave propagation. We also study the run-up in the two fjord settlements of Hellelyst and Geiranger, using Coulwave and MOST coupled with GloBouss (Løvholt et al., 2010). Comparing the simulations with measured surface elevations in control points elsewhere in the scale model, we ensure that the propagating wave and run-up roughly comply with observations. Scale effects and lack of suitable velocity measurement data did represent limiting factors in the analysis. Therefore, it is strongly emphasized that the primary aim of this work is to compare effects of different parameters and model formulations rather than accurately reproducing the laboratory data of Lindstrøm et al. (2014).

## 2 Employed Boussinesq models

We introduce a Cartesian coordinate system with horizontal axes  $ox$  and  $oy$  in the undisturbed water level and an  $oz$  axis pointing vertically upward. The equilibrium depth is denoted by  $h$ , the surface elevation by  $\eta$ , and the velocity components by  $u$  and  $v$  in the  $x$  and  $y$  directions, respectively. We identify a typical depth,  $d$ , a typical wavelength,  $L$ , and an amplitude factor,  $\epsilon$ , that corresponds to a characteristic value of  $\eta/d$ . Different long-wave equations can be obtained through perturbation expansions in  $\mu \equiv d/L$  and  $\epsilon$ . They may then be classified according to which orders these parameters are retained in the equations, when the equations are scaled such that the leading order is unity. The residual (error) terms of the standard Boussinesq equations, such as solved in the early Boussinesq models (Peregrine, 1967), are  $O(\epsilon \mu^2, \mu^4)$ . The primary unknowns then were the surface elevation and the vertically averaged horizontal velocity. Several other formulations with different choices of primary unknowns do exist, of which that of Nwogu (1993) has become widely used. In this formulation the velocity at a chosen depth  $z_\alpha$  is used as a primary unknown. With the optimal choice  $z_\alpha = -0.531 h$ , improved linear dispersion properties are obtained (good for wavelengths down to 2 h, say). Furthermore, Wei et al. (1995) presented a fully nonlinear version of Nwogu's formulation, with residual terms akin to  $O(|\nabla h| \mu^4, \mu^6)$ . In the present paper, various kinds of operational models retaining the residual terms to different degrees, based on the Boussinesq equations of the types listed above, are tested with respect to their ability to model tsunamis in fjords.

## 2.1 Fully nonlinear operational model with run-up – Coulwave

The Coulwave long-wave model was first developed as a means to investigate waves generated by submarine landslides and numerically was very similar to the initial versions of the FUNWAVE model by Wei et al. (1995). Recently, the numerical scheme has been changed to utilize a finite-volume (FV) method for the Boussinesq equations in conservative (flux) form including TVD limiters (Kim et al., 2009). Various turbulence and rotational effects have also been included (e.g., Kim and Lynett, 2011), but these features are not utilized here. Coulwave supports several different drying–wetting formulations (Lynett et al., 2010), and we here employ a centered run-up formulation (see e.g., Løvholt et al., 2013). The centered formulation is preferred due to better robustness and stability properties than the other formulations at the expense of accuracy. On the open boundaries, a sponge layer is utilized. Unless otherwise stated, we run the fully nonlinear, fully dispersive FV version of the Coulwave model with a moving shoreline allowing for inundation. In certain occasions we also run the model assuming a fixed shoreline position or using a non-dispersive (NLSW) version to address the model parameter sensitivity. In the special case of NLSW, we employ a numerical finite difference formulation (Lynett et al., 2002).

A simplified internal source function based on measured surface elevations  $\eta_{\text{lab}}$  from wave gauges in the Åknes scale model (Fig. 1) is employed:

$$\eta_{cw}(x, y, t) = \alpha \cdot \Delta t \sum_{i=1}^n e^{-\beta \Delta y_i'^2} \cdot W_i(x_i') \cdot \eta_{\text{lab},i}. \quad (1)$$

Here,  $\eta_{cw}$  is the surface elevation in the numerical model, and  $\alpha$  and  $\beta$  are parameters that were tuned to provide a reasonable overall agreement with measurement data at the downstream gauge points. Dimensions of  $\alpha$  and  $\beta$  are given in  $\text{s}^{-1}$  and  $\text{m}^{-2}$ , respectively. The summation indicates contributions from each of the gauge points  $i$ . For each gauge point, a dimensionless bi-linear weight function  $W_i$  was employed along the orientation axis  $x_i'$  between two adjacent gauge points, i.e., being unitary at point  $i$  and decaying linearly to points  $i - 1$  and  $i + 1$ . Along the normal direction,  $y_i'$ , we applied the exponential weighting function. Thus, the formulation allows for including different time series gauges as a forcing function for the local numerical solution. Corresponding velocities were not available from the measurements. However, it is stressed that our emphasis is mainly to study differences in model assumptions rather than reproducing the full details of the measured wave field.

Courant numbers of 0.1 were employed for the NLSW simulations and 0.2 for the dispersive. A spatially uniform friction factor  $f = 0.005$ , proportional to the square current velocity times inverse total water depth, was used (see Lynett et al., 2002; Lynett, 2006, for details). As noted by Lynett

et al. (2010), current velocities may become very large for small total water depths and may cause instabilities. To counteract this, Lynett et al. (2010) included a required minimum water depth needed to enable non-zero fluxes. Here, different minimum depths  $h_m$  are applied for different simulations. For the simulations covering the full bathymetry (using the B-bridge for the internal source function) we used a value of  $h_m = 0.002$  m. For the dedicated run-up simulations in Coulwave (using the D- and F-bridges for the internal source function) we could employ a smaller minimum depth of  $h_m = 0.001$  m. We used a transport-based breaking criterion, a procedure adding advection to the conventional breaking model of Kennedy et al. (2000). For details related to the transport-based breaking method see Løvholt et al. (2013).

## 2.2 Mildly nonlinear model for offshore wave propagation – GloBouss

GloBouss is a finite difference model formulated using the optimized standard Boussinesq equations (Pedersen and Løvholt, 2008; Løvholt et al., 2008), i.e., with dispersion properties identical to those of Nwogu (1993) and with second-order nonlinear terms. It is simpler, less demanding, and less computationally intensive than Coulwave and may also be run both in linear shallow water or linear dispersive mode. Like Coulwave, we employ GloBouss with sponge layers over the open boundaries (the northern part of the fjord depicted in Fig. 1 is also treated as open). This makes the model suitable for investigating the importance of the different features of the wave propagation. Here, GloBouss is run using the initial conditions provided from Coulwave using the tapered time series after  $t = 5.07$  s and  $t = 7.10$  s (see Sec. 3.1).

GloBouss does not include drying–wetting and breaking formulations, which are needed for simulating run-up. In their absence, nonlinear terms in the Boussinesq models may lead to instability if the sea bottom is exposed during simulation. This problem is especially severe in the generation area but also for waves entering shallow water near to shore. Such problems are often handled numerically by incorporating a so-called threshold depth. Implementation of such techniques is done either by replacing the data for the part of the bathymetry with depth smaller than the threshold value with the threshold value itself or by moving the shoreline to the threshold depth. Here we have applied the first type with a threshold depth of 0.1 m.

Although GloBouss does not include moving shoreline and shock-capturing facilities by itself, it is set up with a one-way nesting facility with the inundation model MOST (Titov and Synolakis, 1995, 1998). The surface elevation and velocities from GloBouss are fed into MOST during the simulation over the boundaries (see Løvholt et al., 2010, for details). The nesting is utilized below and enables us to simulate the run-up in certain domains of interest such as Hellesylt and Geiranger. Here, MOST is run with the standard Man-

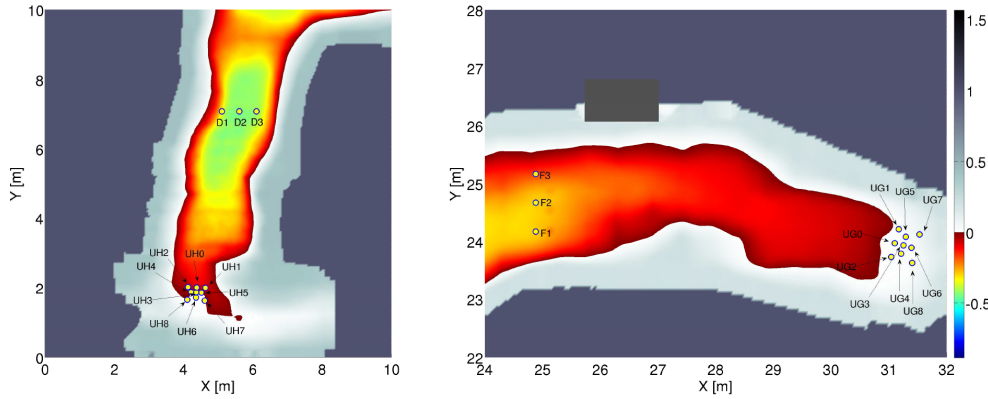


**Figure 2.** Left panel: location of the time series gauges for run-up computation in Hellesylt. Right panel: location of the time series gauges for run-up computation in Geiranger.

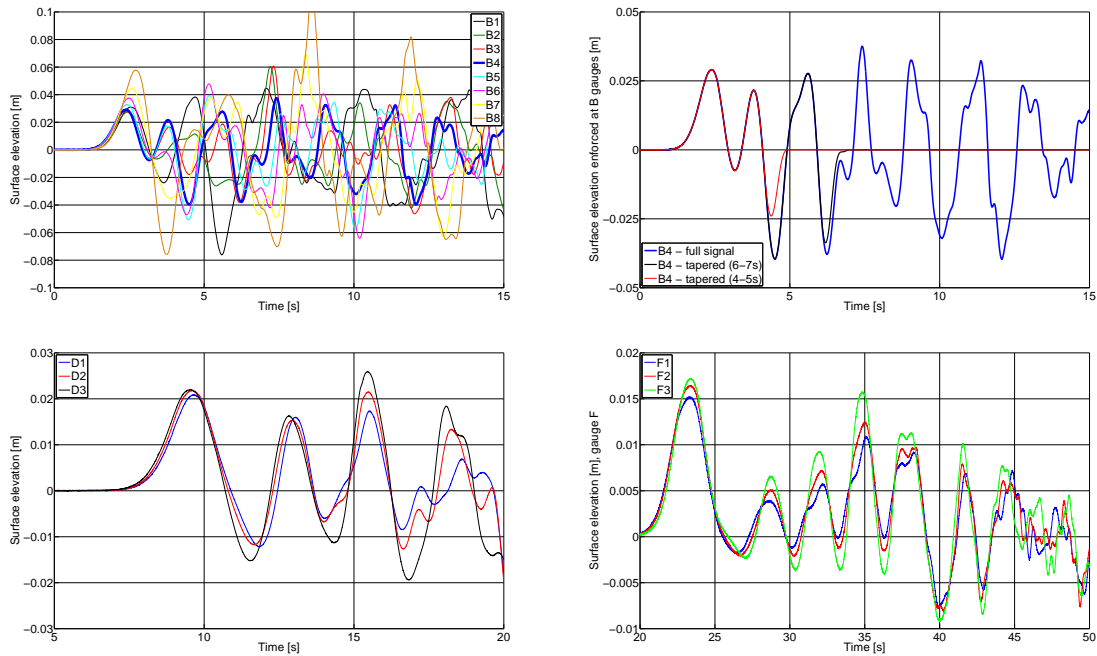


**Figure 3.** Upper left panel: measured surface elevations for the all the wave gauges at the B-bridge. Upper right panel: the tapered B4 signals that were used to provide input to the Coulwave simulations compared to the non-tapered signal. Lower left panel: measured surface elevations for all the wave gauges at the D-bridge. Lower right panel: Measured surface elevations for all the wave gauges at the F-bridge. All measurement data are taken from Lindstrøm et al. (2014).

ning friction parameter of  $n = 0.03$  and a minimum depth of  $h_m = 0.002$  m.

### 3 Tsunami simulations in a scaled model fjord geometry

#### 3.1 Model setup

The simulations were carried out using a processed Lidar scan of the 1 : 500 scale model of the southern part of Stor-fjorden (Fig. 1). The surface elevation and flow depth measurements of Lindstrøm et al. (2014) were extensively used

as input data for the numerical models and for comparison with simulations. The surface elevation measurements utilized herein include resistance probes located along the bridges labeled B, C, D, F, and G; a subset of these are depicted in Fig. 1. In addition, measured flow depths retrieved from acoustic gauges UH0-8 and UG1-8 in Hellesylt and Geiranger were used for comparison with simulated inundation in these two locations (see Fig. 2). A more complete description of all the measurements in the 1 : 500 scale model is given in Lindstrøm et al. (2014).

The objectives of the wave simulations were twofold. The first was to ensure that the main wave characteristics from the laboratory measurements of Lindstrøm et al. (2014) were reproduced in the simulations. For this purpose, Coulwave simulations were compared against wave measurements. The second was to quantify model sensitivity to wave parameters such as the grid resolution, shoreline treatment, nonlinearity, and dispersion on the wave propagation and run-up. Here, we compared Coulwave, GloBouss, and MOST for different parameter combinations using the same initial conditions.

Time series from three different bridges, B, D, and F (Fig. 3), were used to provide input to Coulwave using the internal source function (Eq. 1). While the leading wave for gauges C–G were relatively coherent, propagating mainly along the fjord, signals display phase variations already in the first wave cycle across the B-bridge. Using all the different gauges (B1–B8) set up strong artificial waves across the fjord due to the lateral phase variations. The B4 time series was therefore used to provide joint inputs both for the Coulwave and GloBouss models. Located centrally in the fjord, B4 was considered fairly representative for the deep-water propagation. We use three versions of the B4 time series as a forcing function for the Coulwave simulations (see Fig. 3, upper right panel):

- the B4 full time series assigned to all B-gauges
- B4 tapered between 4 and 5 s, assigned to all B-gauges; instantaneous flow fields  $\eta$ ,  $u$ , and  $v$  from Coulwave were retrieved at  $t = 5.07$  s (Fig. 4, upper panel)
- B4 tapered between 6 and 7 s, assigned to all B-gauges; instantaneous flow fields  $\eta$ ,  $u$ , and  $v$  from Coulwave were retrieved at  $t = 7.1$  s (Fig. 4, lower panel).

The instantaneous fields generated using the tapered signals were used as initial conditions for the GloBouss simulations, thus enabling comparison between the results obtained by Coulwave and GloBouss. The tapering did not affect the leading wave evolution substantially (see the results below). For bridges D and F, phase differences were much less pronounced, and hence the three time series (D1–3 and F1–3) across these two bridges were utilized as forcing conditions. As the time series gauges were aligned along almost straight lines, smooth input conditions were obtained. Values of  $\alpha$  and  $\beta$  were set to, respectively,  $1.67 \text{ s}^{-1}$  and  $17.8 \text{ m}^{-2}$  for bridges B and F and  $0.41 \text{ s}^{-1}$  and  $15.6 \text{ m}^{-2}$  for bridge D. An overview summarizing the purpose, location, use of input data, and models used for the different cases is given in Table 1.

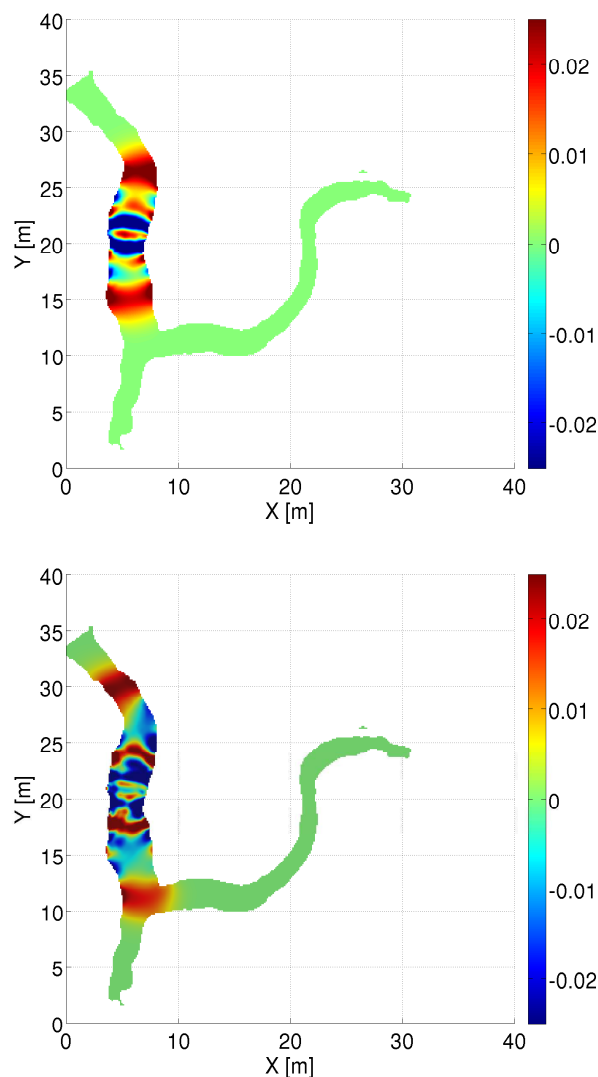


**Figure 4.** Initial surface elevations after wave gauge input data along the B-bridge have been tapered off. Upper panel: surface elevation after  $t = 5.07$  s (B4 signal tapered between 4 and 5 s). Lower panel: surface elevation after  $t = 7.1$  s (B4 signal tapered between 6 and 7 s).

### 3.2 Comparing the Coulwave simulations with measured laboratory data

#### 3.2.1 Fjord propagation

Figure 5 compares the simulated surface elevations using Coulwave with measurements (Lindstrøm et al., 2014) at the four different time series locations: C2, D2, E2, and G2. We have used three different signals as input conditions at the B-bridge: the two tapered signals of B4 and a non-tapered signal. The comparisons show that using the non-tapered signal and the signal tapered at  $t = 7.10$  s provides more or less identical results for at least the first 4–5 wave cycles. These two simulations also provide a somewhat better fit to

**Table 1.** Overview of the models, objective, source input data, and locations for the different case studies in this paper. The different studies comprised of measurement comparisons, grid refinement tests, and model comparisons. The abbreviation CW refers to Coulwave.

Objective	Study type	Study area	Input data	CW	GloBouss	MOST	Section
Measurement comparisons	Wave propagation	Storfjorden	B4 (full)	Y	N	N	3.2.1
Measurement comparisons	Wave propagation	Storfjorden	B4 4–5 s	Y	N	N	3.2.1
Measurement comparisons	Wave propagation	Storfjorden	B4 6–7 s	Y	N	N	3.2.1
Measurement comparisons	Inundation	Hellesylt	D (all)	Y	N	N	3.2.2
Measurement comparisons	Inundation	Geiranger	F (all)	Y	N	N	3.2.2
Grid refinement	Wave propagation and inundation	Storfjorden	B4 6–7 s flow fields	N	Y	N	3.3.1
Model comparisons	Wave propagation	Storfjorden	B4 4–5 s flow fields	Y	Y	N	3.3.2
Model and measurement comparisons	Inundation	Hellesylt	B4 6–7 s flow fields	Y	Y	Y	3.4
Model and measurement comparisons	Inundation	Geiranger	B4 6–7 s flow fields	Y	Y	Y	3.4

the measurements compared to simulations using a signal tapered at  $t = 5.07$ . The simulations generally compare well with the first wave and capture the main trends in the preceding amplitudes and wave periods despite the clearly visible offsets. We therefore find that the tapered input conditions should provide realistic input conditions for the model comparisons, which is the emphasis of the present study.

A uniform grid resolution of  $\Delta x = \Delta y = 0.126$  m was employed (which corresponds to a resolution of 63 m in full scale). In the present setting, model instability arose when the grid resolution was refined further. As demonstrated below by the grid refinement study using the GloBouss model, the present grid resolution is considered adequate for the first 1–2 wave cycles (3–4 % accuracy for the leading crest height for this resolution) but becomes inaccurate for the trailing waves.

### 3.2.2 Near-shore propagation and inundation

Figure 6 compares the simulated surface elevations and flow depths using Coulwave with the measurements by Lindstrøm et al. (2014) at four different time series locations in Hellesylt. Two different grid resolutions 0.11 and 0.056 m were used. A relatively good match with the measured time series was obtained for the first run-up for all points. The main trends in the trailing waves are also captured, although clearly less accurately. While the offshore points show good convergence, deviations between the different grid resolutions are evident for the onshore points.

Figure 7 compares the simulated flow depths using Coulwave with measurements (Lindstrøm et al., 2014) at four different time series locations in Geiranger. Two different grid resolutions 0.126 and 0.063 m were used. Here, the simula-

tions match the measurements less accurately than in Hellesylt, particularly for two of the innermost locations (UG5–6). While the overall trend in the time series is captured at the finest resolution, the simulations show that both employed resolutions are probably too coarse. The runs at finer resolutions were unstable prior to the maximum run-up.

## 3.3 Influence of hydrodynamic parameters on the wave evolution

### 3.3.1 Grid refinement tests

Grid refinement tests were conducted for the GloBouss model, including the nested simulations with MOST. This enabled us to evaluate the accuracy of the models both for the leading and trailing wave systems. Being simpler, GloBouss can be run at higher resolution than Coulwave without encountering instabilities. Although the convergence is monitored mainly for GloBouss, it also gives some indication for Coulwave. The Coulwave simulations presented in this paper are run at the finest resolution allowed by the model to avoid instability.

The convergence is tested by comparing the surface elevation at locations D2 and E2 and UG1 and UH6 for the propagation phase (GloBouss) and run-up (MOST), respectively (see Figs. 8–9). For the propagation phase (Fig. 8), the finest resolution we have tested is 0.063 m. The GloBouss model is run in nonlinear optimized dispersive mode. The initial condition is the solution tapered at 7.10 s. For the leading waves, the difference in the surface elevation measured against the finest resolution is ranging from 3 to 4 % for the 0.126 m resolution. From this we may conclude that for the propagation phase the resolution of 0.252 m or finer is sufficient for

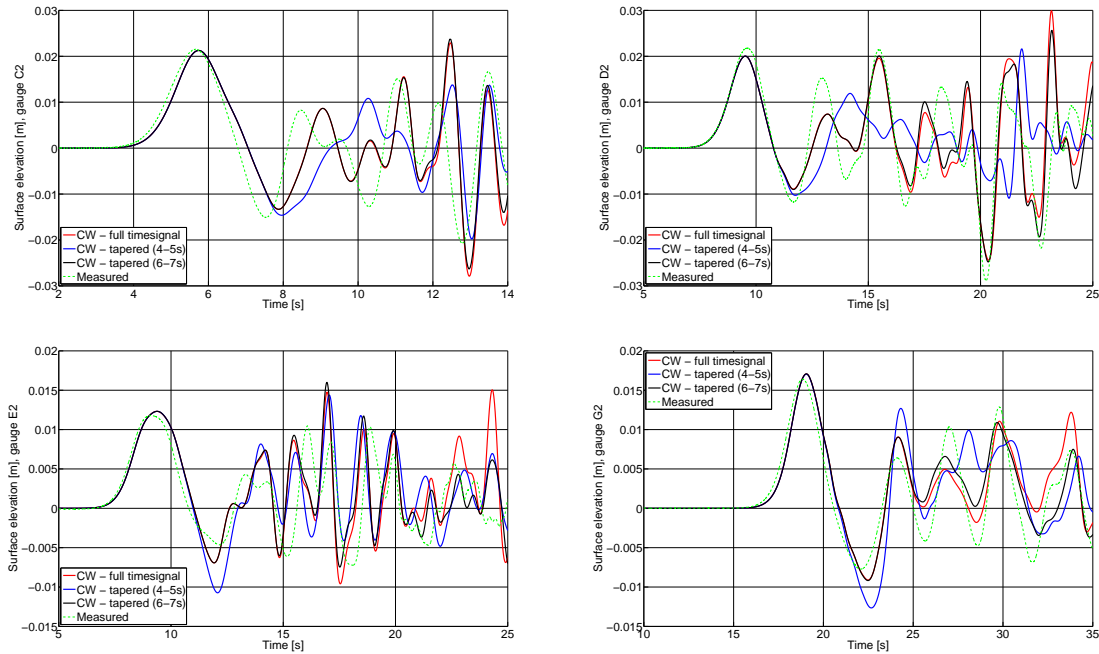


**Figure 5.** Comparison of the simulated surface elevations offshore using Coulwave at central gauges along the C, D, E, and G bridges. The effect of tapering the input signal is demonstrated.

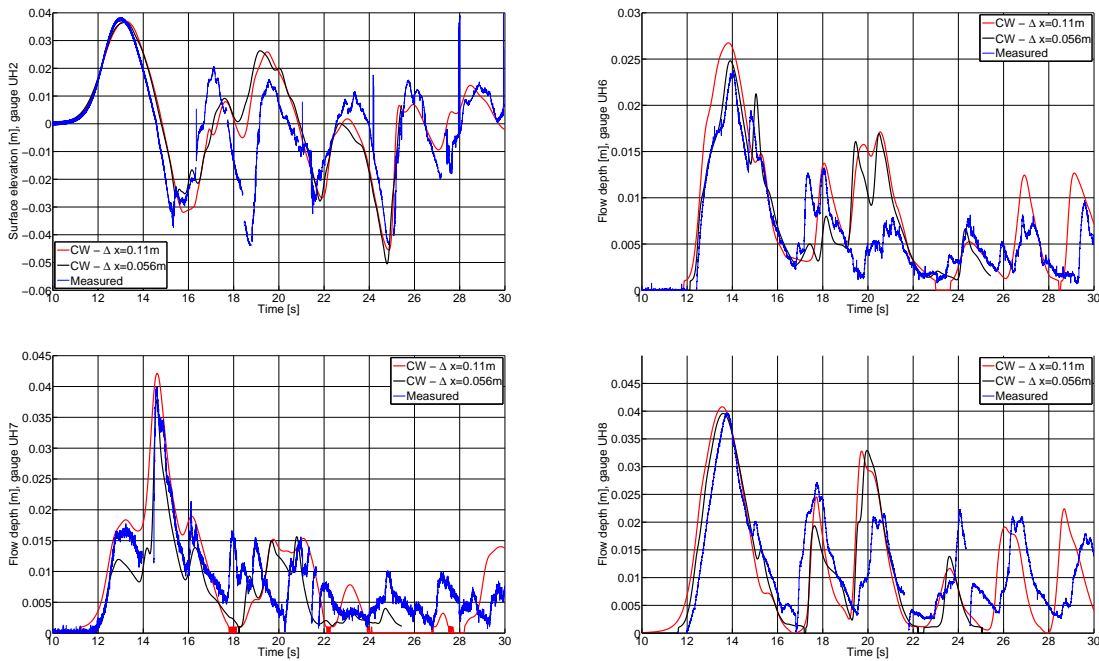


**Figure 6.** Simulated near-shore wave evolution and inundation compared to measured signals at Hellesylt using Coulwave.

proper convergence for the leading wave, and a resolution of 0.126 m is sufficient for the second wave. For the further trailing wave system, we see that even finer resolutions are required for sufficient accuracy. It is noteworthy to see that we are far from obtaining convergence for the trailing wave system even using a “simple” model such as GloBouss at a

fine grid resolution of 0.063 m (corresponding to 31 m in real scale), most likely due to the challenging topography. Furthermore, we note that also GloBouss face instabilities at the highest grid resolution, indicated indirectly by the termination of the blue curve in Fig. 8.

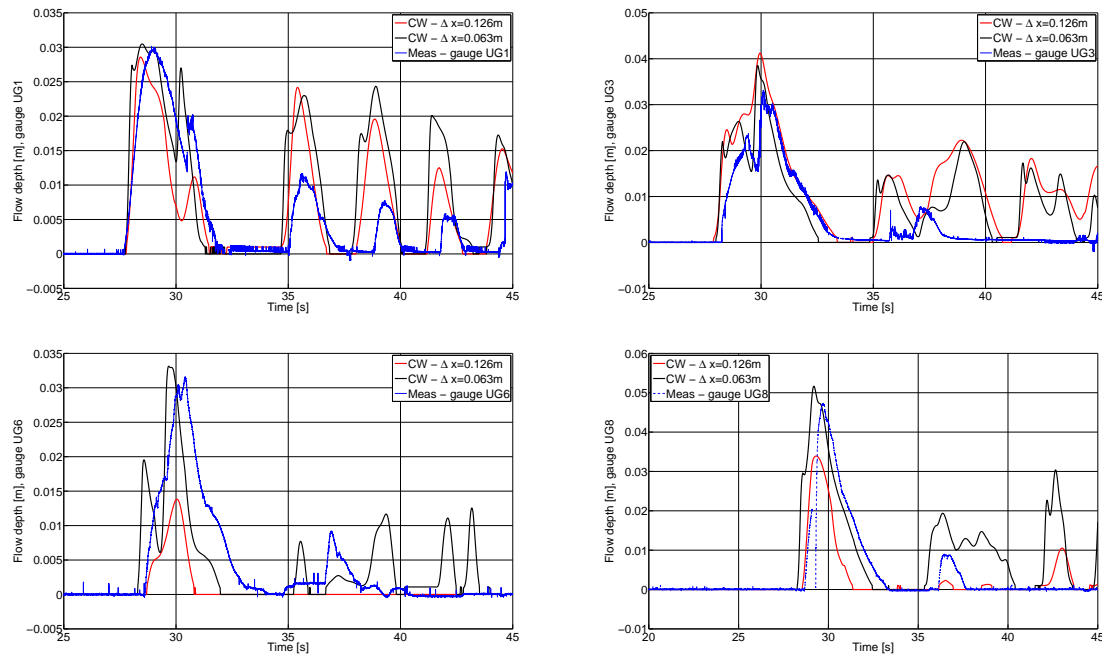


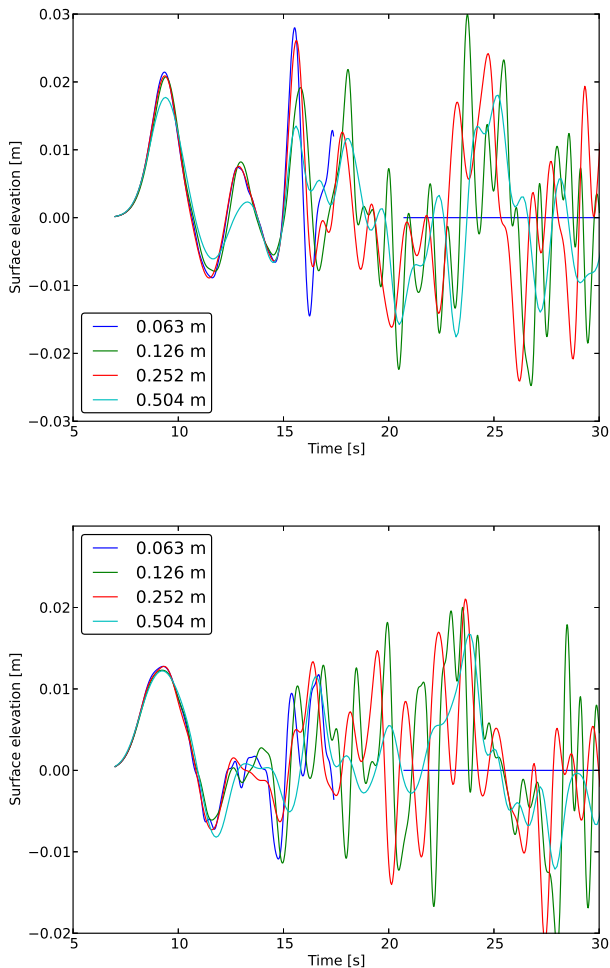
**Figure 7.** Simulated near-shore wave evolution and inundation compared to measured signals at Geiranger using Coulwave.

Grid refinement tests for MOST model nested with GloBouss were conducted for the grid resolutions 0.01, 0.03, and 0.063 m. Flow depths are depicted in Fig. 9. As shown, the solutions seem to converge slowly, with high frequency oscillations at the lowest grid resolution. Hence a high resolution of about 0.03 m is needed for a relatively good convergence, although a resolution of 0.01 m is needed to reproduce the smooth solution evident from the measurements. Both UG1 at Geiranger and UH6 at Hellesylt are located on dry land. For the Coulwave simulations in Hellesylt (see Fig. 6), solutions seems to converge more rapidly; however, corresponding convergence is poor in Geiranger (see Fig. 7).

### 3.3.2 Fjord propagation

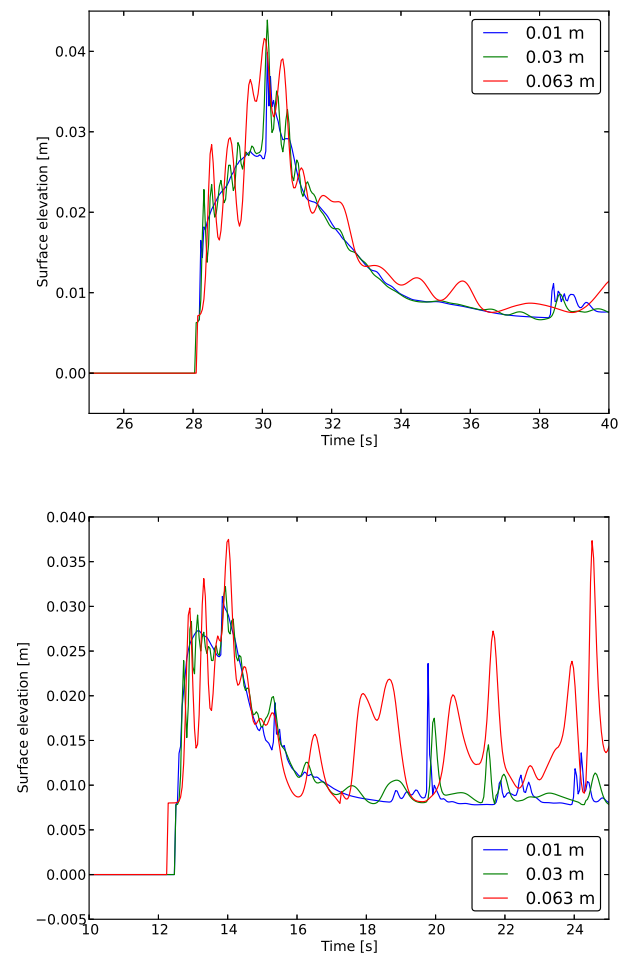
Using the B4 signal tapered at  $t = 5.07$  s we run the Coulwave model for a  $\Delta x = \Delta y = 0.126$  m grid resolution. Simulations were conducted using both the fully dispersive FV model and the FD NLSW model, either with moving or fixed boundaries. In the latter case, use of limiters and shock capturing terms still ensured model stability without alteration of the bathymetry. Correspondingly, GloBouss was run both in nonlinear dispersive and linear mode at identical grid resolution. In both cases, optimized dispersion was used, although higher-order dispersion was found negligible (results not shown). In the absence of breaking and shock-capturing facilities, the bathymetry was altered as described in Sect. 2.2 to ensure model stability. In GloBouss, we use the initial condition produced by the Coulwave model as shown in Fig. 4a.

Figure 10 compares the Coulwave and GloBouss simulations at the four different wave gauges. In the upper two panels, comparisons for relatively short propagation times are depicted at the gauges D2 and E2 located immediately after the fjord T-bend (see Fig. 1). For the leading wave at D2, we find only minor discrepancies between the models where the dispersive terms are retained, with 5 % leading amplitude discrepancy between nonlinear GloBouss and Coulwave. Correspondingly, the linear dispersive GloBouss simulation has a 7 % amplitude discrepancy compared to the nonlinear solution, but the arrival time is clearly shifted. The non-dispersive solution is easily distinguishable from the dispersive, with earlier arrival time and a shorter wave length. However, the non-dispersive solution (labeled NLSW in the figure), provides a surprisingly good fit to the leading wave. For E2, we also see that the leading NLSW solution does not display the smooth shape that is typical due to dispersion. For the preceding wave train, individual model differences become more distinct. As expected, the NLSW model generally provides shorter and less regular wave components than the models containing dispersion. Higher-amplitude waves are found in the wave train resulting from the linear dispersive simulations. In the Coulwave simulations with fixed shoreline, the wave is clearly more damped than for the case with moving shoreline, which may indicate that invoked breaking terms provide additional dissipation. Running the GloBouss model (without dissipation) the opposite is obtained, namely somewhat higher waves. In other words, there is a tendency for the nonlinear dispersive Coulwave simulations to provide somewhat smaller amplitude wave trains



**Figure 8.** Convergence tests for tsunami propagation using GloBouss. The figure shows the surface elevation (mariograms) at gauges D2 (upper panels) and E2 (lower panels) as a function of time. The labels refer to the resolution of each simulation. We note that for the blue curve (finest resolution), the simulation is terminated after about 17 s due to instability.

than the GloBouss model. We may not immediately recognize where the discrepancies originate from, but one possibility is that Coulwave is more dissipative than GloBouss in terms of the breaking and frictional terms, shock capturing, and numerical dissipation (time stepping). For the two time series gauges located at the more distant downstream locations G2 and F2, model differences are also more distinguishable for the leading wave train. First, it is clear that both the NLSW and the linear solutions deviate substantially from the Boussinesq formulations, clearly indicating that both nonlinear and dispersive terms should be accounted for. However, the NLSW model is still reproducing the leading wave rather well, although a slightly too early arrival time and a too large amplitude are found. Second, the observed model differences between Coulwave (including inundation) and GloBouss (without inundation) are moderate, with typi-

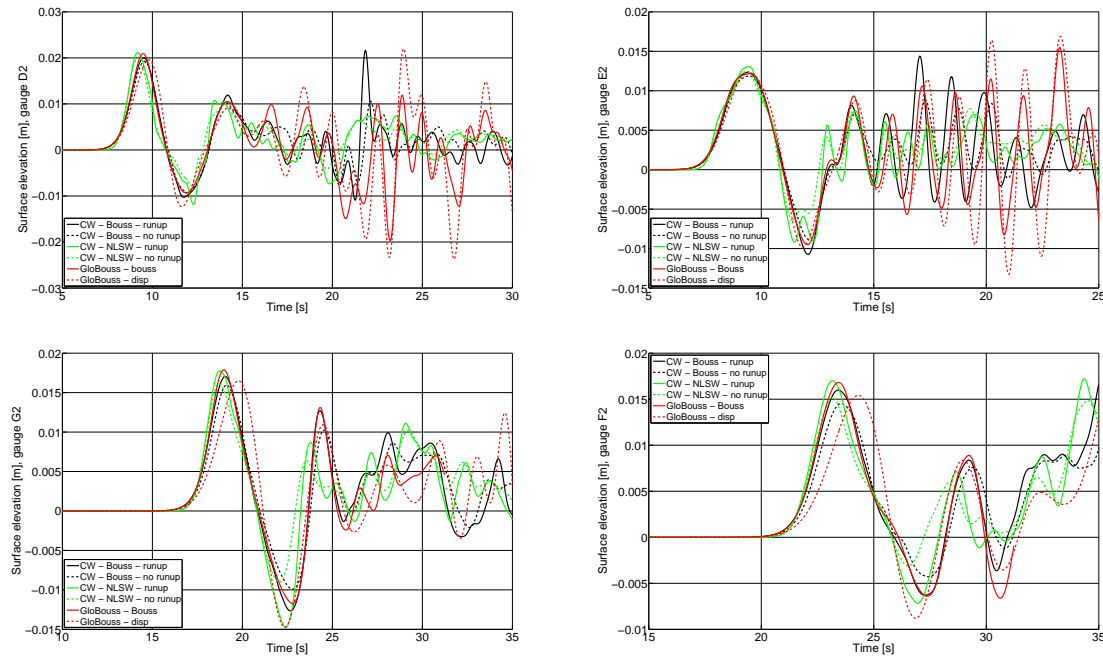


**Figure 9.** Convergence tests for tsunami inundation using MOST (nested with GloBouss). The surface elevation (mariograms) at gauges UG1 (upper panels) and UH6 (lower panels) is given as a function of time. The labels refer to the spatial grid resolution of each simulation.

cal amplitude deviations of 5 % for the leading wave. Therefore, run-up and dissipative effects seem to influence the wave propagation along the fjord basin but are less significant than nonlinearity and dispersion for the leading wave.

### 3.4 Run-up in Hellesylt and Geiranger

Using the simulation tapered at  $t=7.1$  s, we simulate the run-up using both Coulwave and MOST (nested with GloBouss) in Hellesylt and Geiranger. Figure 11 compares the simulated flow depths for the two models with measured data at the Hellesylt location. For Hellesylt, the topographic elevation is much less than the maximum flow depth at UH7–8 (approximately 0.001 m) other than at point UH6 where the topographic elevation is 0.0078 m (point UH0 is located off-shore). As shown, both models estimate the first arrival of measured flow depth and surface elevation data well. However, Coulwave tends to match the trailing waves better.



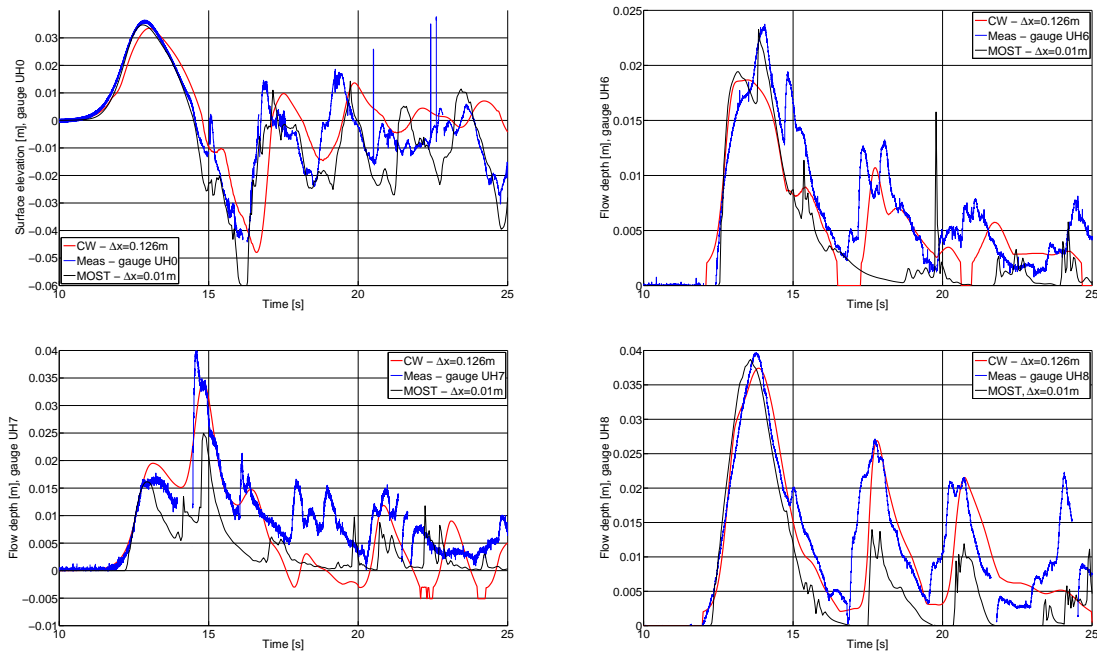
**Figure 10.** Comparison of the simulated surface elevations for Coulwave and GloBouss under different modeling assumptions. The abbreviation “CW” refers to the use of Coulwave; “Bouss” refers to the inclusion of both nonlinear and dispersive terms in the numerical model; “disp” refers to running the model in linear dispersive mode.

Figure 12 compares the simulated flow depths for the two models with measured data at the Geiranger location. Here, the topographic elevation at the control points ranges from 0.019 to 0.027 m, i.e., on the same order of magnitude as the maximum flow depths. In general, both models largely underestimate the inundation in the Geiranger location and, to a even greater extent, the local water depth for the overland flow. However, the differences between simulated and measured maximum inundation (not flow depth) are still smaller than 50 % in most cases and hence somewhat less dramatic than it appears from direct inspection of Fig. 12. The discrepancies are distinctly larger than for the corresponding Coulwave simulations where the model is driven by more local input at the F-bridge. Hence some of the discrepancies may be carried from the offshore simulations in Coulwave and GloBouss and not solely due to the run-up simulations themselves. For the case in Fig. 7 (where local data are used), we are able to use a finer grid resolution and a smaller minimum depth, and the effect of increased accuracy with resolution is clear. The good correspondence between the measurements and simulations at the closest location (G2, Fig. 5) indicates the wave input is fairly well represented and may suggest that the limited resolution (in both grid and minimum depth) is a strong contributor for the lack of agreement with data. Ultimately, it appears that the lack of agreement in Geiranger is due to a variety of factors, but it is clear that a coarse grid resolution and a large minimum depth are important. Compared to Hellesylt, Geiranger is also more demanding in the sense

that the gauge locations are located further onshore and the wave propagation distance prior to the inundation along the fjord is longer.

#### 4 Conclusions

The present analysis has demonstrated the ability (and lack thereof) of Boussinesq models and long-wave solvers in general to tackle the demanding conditions imposed by simulating the tsunami propagation in the narrow and steep-sloping fjord system. We have used surface elevation measurements as input to the numerical simulations. The comparison with the wave measurements offshore has demonstrated that modeled overall characteristics such as amplitudes and wave periods are in place. Because the waves (particularly the trailing ones) have different directivity, and particle velocities measurements are lacking, improved match with data is presently difficult. However, the main purpose of this paper is to demonstrate how hydrodynamic effects influence wave propagation and run-up for characteristic wave patterns imposed by subaerial landslides in fjords. The influence of the alongshore inundation on the propagating wave has been of particular interest. Our findings suggests that the far-field propagation of landslide induced tsunamis are moderately influenced by both nonlinearities and dispersion. The leading wave is surprisingly well described by the nonlinear shallow water model, whereas the dispersion is clearly important for the trailing waves. We further find that inundation influences the alongshore propagation, although the effect is



**Figure 11.** Simulated near-shore wave surface elevation and overland flow depth in Hellesylt for Coulwave and MOST.

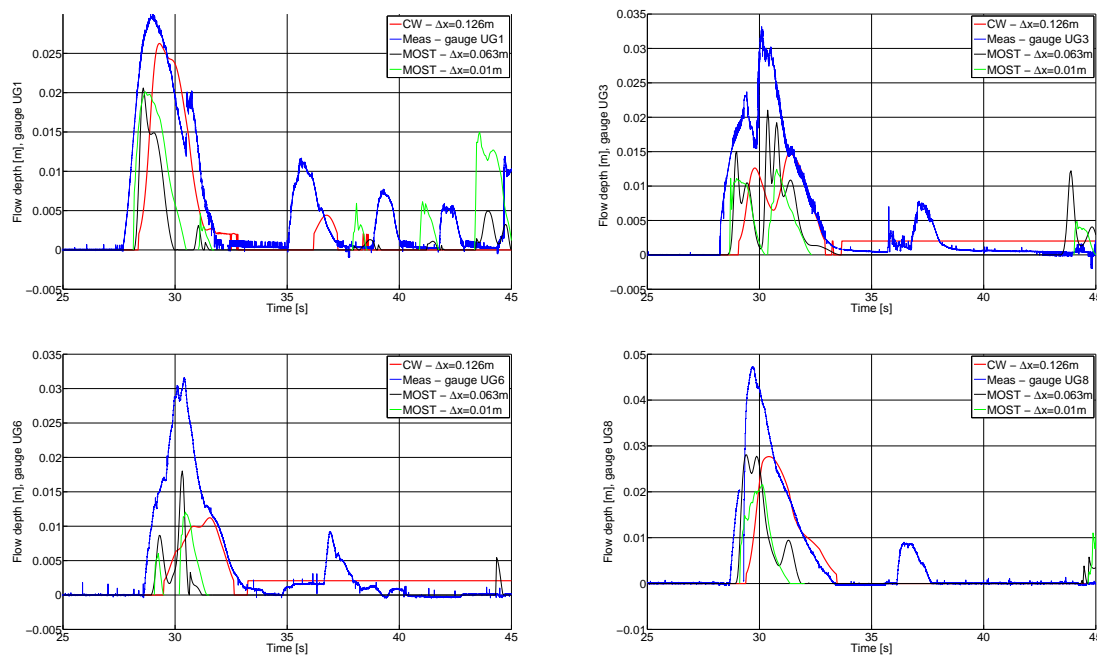


**Figure 12.** Simulated near-shore wave surface elevation and overland flow depth in Geiranger for Coulwave and MOST.

not very strong. As for the dispersion, the inundation seems to affect the trailing waves stronger than the leading wave. Comparing the trailing waves due to the two models, we see that Coulwave involves more dissipation than GloBouss.

The grid resolution needed to reproduce similar waves as those imposed from the laboratory measurements are given considerable attention. From a grid refinement test we find

that the resolution needed for the leading wave is at least 0.252 m, which corresponds to 125 m in real scale. For the trailing wave system, requirements are much stricter: the first 1–2 waves converge for a grid resolution of 0.126 m, while the preceding waves demand a higher resolution for convergence. This poses a problem for the Boussinesq models, particularly fully nonlinear operational models, as instabilities

at high resolution are prominent. The instabilities appear at fine resolution and limit our ability to refine the grid resolution as many times as we would like. We also need to include standard stabilizing factors, such as the minimum depths, that may also limit the accuracy. In any case, the lack of clear convergence for the trailing wave at 0.063 m (31 m in real scale) resolution using our simplest model (GloBouss) suggests that this bathymetry is demanding with respect to modeling the trailing components accurately. Due to the above reasons, our present ability to accurately model the wave train from tsunamis propagating in fjords is somewhat limited. However, the leading wave which is governing the run-up is well represented in the wave propagation simulations.

Simulated near-shore tsunami propagation and inundation at the Hellesylt location, with relatively short inundation distances, compare favorably with the measurements. The model convergence is also good at this location. Inundation simulations in the Geiranger location compare less favorably with the data and convergence is poorer. The most likely reasons for the larger offsets between the measurements and simulations are the limitations in applied grid resolution and the relatively large minimum depths employed. Seemingly more robust, MOST is able to simulate run-up at higher resolution without encountering instabilities. Comparing the two models, however, we see that Coulwave matches the flow depth equally well as MOST even at lower resolution. Compared to the offshore control points, however, the inundation measured onshore is likely to be more strongly affected by scale effects (see Pedersen et al., 2013, for a discussion of scale effects on tsunami run-up). The viscous effects and wave breaking may for instance be influenced by the scaling, and a close correspondence may not be expected for the overland flow. Furthermore, the friction affects the run-up (see e.g., Kaiser et al., 2011; Denissenko et al., 2014).

*Acknowledgements.* The work has been funded by the Research Council of Norway projects “Laboratory experiments and numerical modeling of tsunamis generated by rock slides into fjords” (NFR 205184/F20) and “Tsunamis induced by large landslides” (NFR 231252/F20) as well as by NGI. We also thank Erika Lindstrøm for providing and adapting measurement data for use in the numerical simulations. Finally, we thank Alberto Armigliato and one anonymous referee for their helpful comments on the first version of this manuscript.

Edited by: A. Armigliato

Reviewed by: A. Armigliato and one anonymous referee

## References

Blikra, L., Longva, O., Harbitz, C., and Løvholt, F.: Quantification of rock-avalanche and tsunami hazard in Storfjorden, western Norway, in: *Landslides and Avalanches, ICFL 2005, Norway, Senneset*, edited by: Senneset, K., Flaate, K., and Larsen, J. O., Taylor & Francis, London, UK, 57–64, 2005

- Denissenko, P., Pearson, J., Rodin, A., and Didenkulova, I.: Long waves climbing the slopes of different roughness: run-up height and the load on individual roughness elements, in: *Proceedings of the Hydralab Joint User Meeting, Lisbon, July, 2014*.
- Erduran, K., Ilic, S., and Kutija, V.: Hybrid finite-volume finite-difference scheme for the solution of boussinesq equations, *Int. J. Num. Meth. Fluids*, 49, 1213–1232, 2005.
- Fritz, H., Hager, W. H., and Minor, H.-E.: Near field characteristics of landslide generated impulse waves, *J. Waterw. Port, Coastal, Ocean Eng.*, 130, 287–302, 2004.
- Harbitz, C. B., Glimsdal, S., Løvholt, F., Kvelde, V., Pedersen, G., and Jensen, A.: Rockslide tsunamis in complex fjords: from an unstable rock slope at Åkerneset to tsunami risk in western Norway, *Coast. Eng.*, 88, 101–122, 2014.
- Harbitz, C. B., Pedersen, G., and Gjevik, B.: Numerical simulation of large water waves due to landslides, *J. Hydraul. Eng.*, 119, 1325–1342, 1993.
- Heller, V., Hager, W., and Minor, M.: Scale effects in subaerial landslide generated impulse waves, *Exp. Fluids*, 94, 691–703, 2008.
- Imamura, F.: Review of tsunami simulation with finite difference method, in: *Long-Wave Runup Models*, edited by: Yeh, H., Liu, P., and Synolakis, C., World Scientific Publishing Co., Singapore, 25–42, 1996.
- Jørstad, F.: *Waves Generated by Slides in Norwegian Fjords and Lakes*, Institute publication 79, Norwegian Geotechnical Institute, 1968.
- Kaiser, G., Scheele, L., Kortenhaus, A., Løvholt, F., Römer, H., and Leschka, S.: The influence of land cover roughness on the results of high resolution tsunami inundation modeling, *Nat. Hazards Earth Syst. Sci.*, 11, 2521–2540, doi:10.5194/nhess-11-2521-2011, 2011.
- Kennedy, A. B., Chen, Q., Kirby, J. T., and Dalrymple, R. A.: Boussinesq modeling of wave transformation, breaking, and run-up, Part I: 1D, *J. Waterw. Port. Coast. Ocean Eng.*, 126, 39–47, 2000.
- Kim, D.-H. and Lynett, P.: Turbulent mixing and passive scalar transport in shallow flows, *Phys. Fluids*, 23, 016603, doi:10.1063/1.3531716, 2011.
- Kim, D.-H., Lynett, P., and Socolofsky, S.: A depth-integrated model for weakly dispersive, turbulent, and rotational flows, *Ocean Model.*, 27, 198–214, 2009.
- LeVeque, R. J. and George, D. L.: High-resolution finite volume methods for the shallow water equations with bathymetry and dry states, in: *Advanced Numerical Models for Simulating Tsunami Waves and Runup*, edited by: Liu, P. L.-F., Yeh, H., and Synolakis, C. E., Vol. 10, World Scientific Publishing, Third International Workshop on Long-Wave Runup Models, Catalina Island, USA, 43–74, 2008.
- Lindstrøm, E. K., Pedersen, G. K., Jensen, A., and Glimsdal, S.: Experiments on slide generated waves in a 1 : 500 scale fjord model, *Coastal Eng.*, 92, 12–23, doi:10.1016/j.coastaleng.2014.06.010, 2014.
- Løvholt, F. and Pedersen, G.: Instabilities of Boussinesq models in non-uniform depth, *Int. J. Num. Meth. Fluids*, 61, 606–637, 2009.
- Løvholt, F., Pedersen, G., and Gisler, G.: Modeling of a potential landslide generated tsunami at La Palma Island, *J. Geophys. Res.*, 113, C09026, doi:10.1029/2007JC004603, 2008.

- Løvholt, F., Pedersen, G., and Glimsdal, S.: Coupling of dispersive tsunami propagation and shallow water coastal response, *Open Oceanogr. J.*, 4, 71–82, 2010.
- Løvholt, F., Lynett, P., and Pedersen, G.: Simulating run-up on steep slopes with operational Boussinesq models; capabilities, spurious effects and instabilities, *Nonlin. Processes Geophys.*, 20, 379–395, doi:10.5194/npg-20-379-2013, 2013.
- Lynett, P. J.: Nearshore wave modeling with high-order Boussinesq-type equations, *J. Waterw. Port Coast. Ocean Eng.*, 132, 2119–2146, 2006.
- Lynett, P. J., Melby, J., and Kim, D.-H.: An application of boussinesq modeling to hurricane wave overtopping and inundation, *Ocean Eng.*, 37, 135–153, 2010.
- Lynett, P. J., Wu, T.-R., and Liu, P. L.-F.: Modeling wave runup with depth-integrated equations, *Coast. Eng.*, 46, 89–107, 2002.
- Madsen, P. and Sørensen, O.: A new form of the Boussinesq equations with improved linear dispersion characteristics, Part 2. A slowly-varying bathymetry, *Coast. Eng.*, 18, 183–204, 1992.
- Madsen, P., Bingham, H., and Schäffer, H.: Boussinesq type formulations for fully nonlinear and extremely dispersive water waves: derivation and analysis, *Philos. T. Roy. Soc. Lond. A*, 459, 1075–1004, 2003.
- Miller, D.: Giant waves in Lituya Bay Alaska, Geological Survey professional paper 354-C, USGS, United States Government Printing Office, Washington, USA, 1960.
- Nwogu, O.: Alternative form of Boussinesq equations for nearshore wave propagation, *J. Waterw. Port. Coast. Ocean Eng.*, 119, 618–638, 1993.
- Oppikofer, T., Jaboyedoff, M., Blikra, L., Derron, M.-H., and Metzger, R.: Characterization and monitoring of the Åknes rockslide using terrestrial laser scanning, *Nat. Hazards Earth Syst. Sci.*, 9, 1003–1019, doi:10.5194/nhess-9-1003-2009, 2009.
- Pedersen, G. and Løvholt, F.: Documentation of a global Boussinesq solver, Preprint Series in Applied Mathematics 1, Dept. of Mathematics, University of Oslo, Norway, available at: <http://urn.nb.no/URN:NBN:no-27775> (last access: July 2014), 2008.
- Pedersen, G. K., Lindstrøm, E., Bertelsen, A. F., Jensen, A., Laskovski, D., and Sælevik, G.: Runup and boundary layers on sloping beaches, *Phys. Fluids*, 25, 012102, doi:10.1063/1.4773327, 2013.
- Peregrine, D. H.: Long waves on a beach, *J. Fluid Mech.*, 77, 417–431, 1967.
- Plafker, G. and Eyzaguirre, V.: Rock avalanches and wave at Chungar, Peru, Vol. 14B of *Development in Geotechnical Engineering*, Chap. 7, University of California, Elsevier, Amsterdam, 269–279, 1979.
- Sepúlveda, S. and Serey, A.: Tsunamigenic, earthquake-triggered rock slope failures during the april 21 2007 aisen earthquake, Southern Chile (45.5 degrees), *Andean Geol.*, 26, 131–136, 2009.
- Shi, F., Kirby, J., Harris, J., Geiman, J., and Grilli, S.: A high-order adaptive time-stepping tvd solver for Boussinesq modeling of breaking waves and coastal inundation, *Ocean Model.*, 43–44, 31–51, 2012.
- Tinti, S. and Guidoboni, E.: Revision of tsunamis occurred in 1783 in Calabria and Sicily (Italy), *Sci. Tsunami Haz.*, 6, 17–22, 1988.
- Titov, V. V. and Synolakis, C. E.: Modeling of breaking and non-breaking long-wave evolution and runup using VTCS-2, *J. Waterw. Port. Coast. Ocean Eng.*, 121, 308–316, 1995.
- Titov, V. V. and Synolakis, C. E.: Extreme inundation flows during the Hokkaido–Nansei-Oki tsunami, *Geophys. Res. Lett.*, 24, 1315–1318, 1997.
- Titov, V. V. and Synolakis, C. E.: Numerical modeling of tidal wave runup, *J. Waterway Port. Coast. Ocean Eng.*, 124, 157–171, 1998.
- Tonelli, M. and Petti, M.: Shock-capturing boussinesq model for irregular wave propagation, *Coast. Eng.*, 61, 8–19, 2012.
- Wei, G., Kirby, J. T., Grilli, S. T., and Subramanya, R.: A fully nonlinear Boussinesq model for surface waves, Part 1. Highly nonlinear unsteady waves, *J. Fluid Mech.*, 294, 71–92, 1995.